ELECTROCHEMISTRY

Transforming from planar to three-dimensional lithium with flowable interphase for solid lithium metal batteries

Yayuan Liu,[1] Dingchang Lin,[1] Yang Jin,[1] Kai Liu,[1] Xinyong Tao,[1] Qiuhong Zhang,[2] Xiaokun Zhang,[1] Yi Cui[1,3]*

Solid-state lithium (Li) metal batteries are prominent among next-generation energy storage technologies due to their significantly high energy density and reduced safety risks. Previously, solid electrolytes have been intensively studied and several materials with high ionic conductivity have been identified. However, there are still at least three obstacles before making the Li metal foil-based solid-state systems viable, namely, high interfacial resistance at the Li/electrolyte interface, low areal capacity, and poor power output. The problems are addressed by incorporating a flowable interfacial layer and three-dimensional Li into the system. The flowable interfacial layer can accommodate the interfacial fluctuation and guarantee excellent adhesion at all time, whereas the three-dimensional Li significantly reduces the interfacial fluctuation from the whole electrode level (tens of micrometers) to local scale (submicrometer) and also decreases the effective current density for high-capacity and high-power operations. As a consequence, both symmetric and full-cell configurations can achieve greatly improved electrochemical performances in comparison to the conventional Li foil, which are among the best reported values in the literature. Noticeably, solid-state full cells paired with high–mass loading $LiFePO_4$ exhibited, at 80°C, a satisfactory specific capacity even at a rate of 5 C (110 mA·hour g^{-1}) and a capacity retention of 93.6% after 300 cycles at a current density of 3 mA cm^{-2} using a composite solid electrolyte middle layer. In addition, when a ceramic electrolyte middle layer was adopted, stable cycling with greatly improved capacity could even be realized at room temperature.

INTRODUCTION

Lithium (Li)–based rechargeable batteries play a vital role in modern society. They are not only the dominant power source for consumer electronics but also the most prominent energy storage technology for the widespread adoption of electric vehicles on the horizon (1, 2). Nevertheless, it has been generally recognized that batteries with higher energy and power densities are urgently needed to accelerate the electrification of transportation, necessitating battery chemistries beyond the state-of-the-art Li-ion (3, 4). To realize this goal, Li metal is the ultimate anode of choice because it has the highest theoretical capacity (3860 mA·hour g^{-1}) and lowest electrochemical potential (−3.04 V versus standard hydrogen electrode) among all the candidate materials (5). However, the practical applications of the Li metal anode have been severely hindered by the problems of poor cycle life and serious safety concerns, which originated from its high reactivity with organic liquid electrolytes and uneven deposition behavior (dendrites). The latter can potentially incur thermal runaway and explosion hazards by internally short-circuiting the cells (6).

To address the aforementioned challenges and make Li metal anode a viable technology, an attractive strategy is to replace the volatile liquid electrolytes with nonflammable solid counterparts that are electrochemically stable against Li and mechanically robust to suppress dendrite growth (7–9). Although a wide variety of solid electrolytes for Li batteries have been developed throughout the years, ranging from inorganic ceramic electrolytes to solid polymer electrolytes (SPEs) (10–18), the same critical challenge, which is the interfacial detachment between solid electrolytes and electrodes, awaits to be solved for all the systems.

Unlike liquid electrolytes, solid electrolytes barely have any fluidity to form a continuous contact with active materials inside the electrodes. Therefore, the electrochemical process can be severely limited by the contact area, leading to great interfacial resistance and low utilization of electrode capacity (7). The issue is even more pronounced for the Li metal anode, whose interfacial fluctuation (defined as the degree of Li surface movement during cycling) in practical applications can be as large as tens of micrometers (1 mA·hour cm^{-2} corresponds to ~5-μm Li in thickness), making it difficult to cycle the solid-state Li batteries at high capacity and current density. The uneven current distribution due to poor interfacial contact may also promote dendrite growth. Several approaches have been proposed to improve the interfacial adhesion, including plasticizing SPEs with small organic molecules (19–21), constructing interfacial buffer layers (22–24), and using nanostructured block copolymers with liquid-like surface properties (25). However, further research endeavors are still needed along these directions such that good interfacial contact can be realized without compromising the non-flammability, the mechanical properties (known as the "modulus versus adhesion dilemma") (25), or the engineering cost of the solid electrolytes. Noticeably, all the existing strategies are developed on the basis of planar Li foil, which could barely remain effective under high areal capacity cycling due to the drastic interfacial fluctuation, and the current density that planar Li foil could endure is not high enough, impeding the high-power operation of the cells.

Here, we present a paradigm shift on the structural design of solid-state Li batteries: Unlike all the previous studies where solid-state cells were constructed using planar Li foil, we adopted three-dimensional (3D) Li anode with high electroactive surface area for the first time (26–28). Moreover, the challenge of creating a conformal and continuous ionic contact between the 3D Li anode and the bulk solid electrolyte was successfully addressed via a flowable ion-conducting interphase.

[1]Department of Materials Science and Engineering, Stanford University, Stanford, CA 94305, USA. [2]Department of Chemical Engineering, Stanford University, Stanford, CA 94305, USA. [3]Stanford Institute for Materials and Energy Sciences, SLAC National Accelerator Laboratory, 2575 Sand Hill Road, Menlo Park, CA 94025, USA.
*Corresponding author. Email: yicui@stanford.edu

Specifically, metallic Li in layered reduced graphene oxide host (Li-rGO) was used as the anode, and poly(ethylene glycol) [PEG; molecular weight (M_W), 10,000] plasticized by bis(trifluoromethane)sulfonimide Li salt (LiTFSI), which resembles a viscous semiliquid, was impregnated into the 3D Li-rGO via thermal infiltration to construct the flowable interphase. This structural design has several major advantages: first, the adoption of a 3D Li anode significantly increases the electrode-electrolyte contact area, dissipating the current density to facilitate charge transfer and offering the opportunities to high-power operation. Second, by dividing bulk Li into small domains, the interfacial fluctuation during cycling can be reduced to the submicrometer scale, enabling the cells to be cycled at a much higher capacity (26). More importantly, the incorporation of a flowable interfacial layer can accommodate the varying morphology at the 3D Li anode surface during cycling, which is desirable for maintaining a continuous electrode-electrolyte contact. Finally, the 3D Li anode design can be adopted as a general approach in solid-state Li batteries, which is compatible with both SPEs and inorganic ceramic electrolytes. With the above merits, our innovative design allows for the construction of solid-state Li cells with outstanding electrochemical behavior in terms of overpotential and stability in both symmetric and full-cell configurations over a wide range of operating temperatures (demonstrated from room temperature to 80°C). When paired with high–mass loading LiFePO$_4$ (LFP) cathode and a composite polymer electrolyte (CPE), cells constructed using the Li-rGO anode with flowable interphase demonstrated excellent rate capabilities (141 and 110 mA·hour g^{-1} for 1 and 5 C, respectively, at 80°C) and cycle life (93.6% capacity retention after 300 cycles at 80°C with a current density of 3 mA cm^{-2}) that are among the best reported values so far, whereas the Li foil counterparts had only mediocre performance (120 and 60 mA·hour g^{-1} for 1 and 5 C, respectively, at 80°C; 46% capacity retention after 300 cycles at 80°C with a current density of 3 mA cm^{-2}). In addition, stable room temperature cycling was also realized in combination with garnet-type ceramic electrolyte. Therefore, this 3D Li anode with a flowable interphase can shed light on the new architectural design principles of solid Li metal batteries, and it is promising that even better cell performance can be realized when paired with advanced bulk solid electrolyte in the future.

RESULTS AND DISCUSSION
Design strategy of the 3D Li metal anode with flowable interphase
Figure 1 schematically shows the fabrication process of solid Li metal cells based on our novel anode design. There have been various impor-

tant reports recently on stabilizing Li metal with carbon-based host materials, and Li-rGO was used in this study as a demonstration (29, 30). Metallic Li with a thickness of several hundred nanometers can be uniformly stored in between the rGO flakes, according to our previous report (Fig. 1A) (26). Specifically, when densely stacked layered GO film obtained by vacuum filtration is put into contact with molten Li, a "spark reaction" can occur instantaneously, expanding the film into a porous structure (fig. S1A). This can be explained by the sudden pressure release of the superheated residual water molecules within the GO layers and the combustion of hydrogen produced from the partial reduction of the oxygen-containing surface functional groups. Subsequently, when the edge of the sparked film is placed in molten Li, Li can infuse into the rGO host rapidly and homogeneously. The mechanism of the molten Li infusion is explained schematically in fig. S1B. The strong interaction between molten Li and the remaining surface functional groups on rGO makes the rGO surface "lithiophilic" (that is, good molten Li wettability). It is known that the capillary force on a good wetting surface will raise the liquid level, and the height of the liquid level is inversely proportional to the dimension of the gaps. Therefore, the nanoscale gaps between the rGO layers can provide a strong capillary force to drive the molten Li intake into the rGO host. The advantages of the resulting Li-rGO composite structure, including suppressed dendrite formation, largely increased electroactive surface area, enhanced cycling efficiency, and minimum volume change during cycling, have been demonstrated using liquid electrolyte systems (26).

Notably, to construct solid-state cells based on 3D Li, an effective strategy to form continuous ionic percolation throughout the nanosized pores is critically needed, which is challenging to achieve. The highly reactive nature of Li metal with organic solvents severely restricts the possibilities for solution-based solid electrolyte impregnation (31, 32). However, it remains a great technical challenge to realize conformal solid electrolyte coating on 3D Li via gas-phase deposition at temperatures below the melting point of Li (180.5°C) (33, 34). Accordingly, we propose the thermal infiltration of the short-chain polymer electrolyte into Li-rGO, which was specially engineered to be flowable over a wide range of operating temperatures to guarantee an intimate ionic contact (Fig. 1B). The properties of the flowable interphase layer will be described in greater detail in the following section.

After the construction of the high-area flowable interphase layer, as a proof of concept, a mechanically strong CPE (fig. S2) or a cubic garnet-type Li$_{6.5}$La$_3$Zr$_{0.5}$Ta$_{1.5}$O$_{12}$ (LLZTO) ceramic electrolyte was adopted as the bulk solid electrolyte middle layer. Specifically, the CPE consists of long-chain poly(ethylene oxide) (PEO; M_W, 300,000), LiTFSI, and
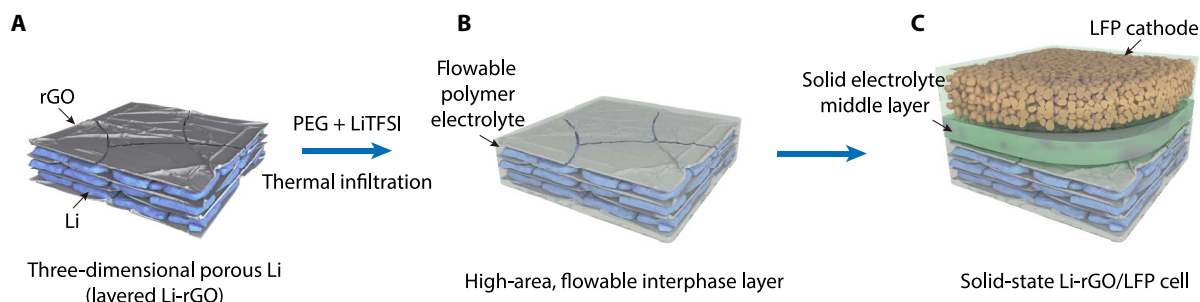

Fig. 1. Schematics illustrating the fabrication process of the 3D Li anode with flowable interphase for solid-state Li battery. (**A**) 3D Li-rGO composite anode was first fabricated. (**B**) A flowable interphase for the 3D Li-rGO anode was created via thermal infiltration of liquid-like PEG-LiTFSI at a temperature of 150°C. (**C**) A CPE layer consisting of PEO, LiTFSI, and fumed silica or an LLZTO ceramic membrane was used as the middle layer, and high–mass loading LFP cathode with the CPE as the binder was overlaid to construct the solid-state Li-LFP full cell.

fumed silica nanoparticles (*35*, *36*). The introduction of the fumed silica nanoparticles in the CPE has the following functionalities: (i) the nanoparticles serve as cross-linking centers to reduce the crystallinity of PEO, facilitating the segmental motions of the polymer chains to increase the ionic conductivity; (ii) the strong Lewis acid-base interaction between the surface chemical groups of the fumed silica nanoparticles (Lewis acid) and the Li salt anions (Lewis base) can promote salt dissociation, which also increases the ionic conductivity; (iii) the rigid silica fillers can enhance the mechanical property of the polymer electrolyte. Therefore, this structural design is also advantageous in the sense that the two conflicting requirements for solid electrolytes, namely, high mechanical property (solid electrolyte middle layer) and good interfacial adhesion (flowable interphase layer), can be successfully decoupled (*25*). Finally, a high–mass loading LFP cathode using the same CPE as binder was overlaid to form the final full cell (Fig. 1C).

Materials characterizations

Figure 2A shows the rheological properties of the flowable PEG polymer electrolyte. Although pure PEG is a semicrystalline solid at room temperature, crystallization can be effectively suppressed in the presence of LiTFSI salt (fig. S3) (*37*). The stability of the liquid-like PEG polymer electrolyte increases with increasing salt concentration, and when the [EO]/[Li] ratio reached 8:1, a viscous gel can be maintained even at room temperature. The complex viscosity of the flowable PEG was measured to be ~55 Pa·s at 20°C but decreased to only ~1.8 Pa·s when heated to 100°C; the viscosity can be even lower at the actual thermal infiltration temperature (~150°C), which is a value beyond the measurement limit of the instrument. Moreover, the loss modulus was higher than the storage modulus at all measured temperatures, indicating the liquid-like behavior of the flowable PEG (fig. S4). The relatively high viscosity at low temperatures imparts the PEG polymer electrolyte limited mobility to diffuse into the bulk solid electrolyte middle layer during operations. However, the good fluidity at elevated temperatures makes it favorable for thermal polymer infiltration into the 3D Li-rGO anode. Scanning electron microscopy (SEM) was used to study the microstructures of the 3D Li-rGO electrode before and after the thermal infiltration of flowable PEG. As shown in Fig. 2B, the pristine Li-rGO anode exhibited uniform stacking of nanoscale Li and layered rGO with high porosity. After flowable PEG infiltration, it is evident that the polymer electrolyte completely occupied the nanoscale pores of Li-rGO (Fig. 2C). This difference can also be observed visually, because the Li-rGO electrode appeared darker in color after thermal infiltration due to the filling of the nanopores (Fig. 2, D and E).

The porosity of the 3D Li-rGO electrode used in this study was measured to be ~39 volume % via mineral oil absorption test (fig. S5A). The subsequent infiltration of flowable PEG resulted in, on average, ~200% increase in the total weight of the composite electrode (fig. S5B, red dot). Given the density of the flowable PEG electrolyte (~1.2 g cm^{-3}), the theoretical weight increase of the electrode with 39 volume % porosity, if completely infiltrated by the electrolyte, is ~150% (blue dot). In addition, there was also a thin layer of flowable PEG covering the surface of Li-rGO; thus, the measured value is reasonable. The specific capacity of the 3D Li-rGO electrode with flowable interphase was determined by stripping the electrode to 1 V versus Li$^+$/Li in a solid-state cell and compared to the value in liquid electrolyte (1 M LiPF$_6$ in 1:1 ethylene carbonate/diethyl carbonate; fig. S6). For Li-rGO with 39 volume % porosity, the specific capacity in liquid electrolyte was ~3170 mA·hour g^{-1}, and when integrated into a solid-state cell with flowable interphase, a high extractable capacity of ~2890 mA·hour g^{-1}

can be retained. This indicates the effectiveness of the flowable interphase in maintaining the ionic contact between the 3D electrode and the bulk solid electrolyte during Li stripping. On the other hand, if the porosity of the Li-rGO electrode was reduced to 15 volume % (by reducing the residual water content in the starting GO film), less capacity can be extracted in the solid-state cell (~2583 mA·hour g^{-1}) together with increased stripping overpotential. Therefore, high Li-rGO porosity is desirable to increase the electrode-electrolyte contact area for better electrochemical performance.

The crystallinity of the polymer electrolytes was further characterized using differential scanning calorimetry (DSC) analysis (Fig. 2F). The absence of endothermic melting peaks in DSC reveals that both the flowable PEG and the CPE middle layer used in this study had an amorphous structure, which is crucial for realizing high ionic conductivity. Correspondingly, their ionic conductivity obtained from the Nyquist plots of electrochemical impedance tests can reach the order of 10^{-4} S cm^{-1} at only around 40°C (Fig. 2G), enabling the operation of solid-state Li cells at only slightly elevated temperature (possibly human body temperature for wearables). Finally, the electrochemical stability window of the solid electrolytes was studied at 80°C via cyclic voltammetry (CV). As can be seen from Fig. 2H, the flowable PEG can be stable up to 5 V versus Li$^+$/Li, and the CPE middle layer also demonstrated negligible anodic decomposition at the potential of the LFP cathode used in the study. In addition, the excellent compatibility with Li metal makes the PEG electrolyte an ideal choice for the buffer layer, interfacing the 3D Li anode and the solid electrolyte middle layer without blocking Li-ion transport (*38*).

Electrochemical testing with symmetric cell configuration

To demonstrate the advantages of our 3D Li-rGO anode with flowable interphase, electrochemical characterizations in symmetric cell configuration with CPE middle layer were carried out and compared with the conventional Li foil counterpart. The thickness of the 3D Li-rGO used was ~100 to 150 μm, and the value could be easily tuned by changing the thickness of the rGO host to vary the mass loading of the anode (fig. S7), whereas the thickness of the reference Li foil was 750 μm. The mass of the 3D Li-rGO electrode was ~4 to 5 mg cm^{-2}, given the measured specific capacity of the electrode discussed above (fig. S6; ~2890 mA·hour g^{-1} based on the weight of Li-rGO), and the areal mass loading of the 3D Li-rGO anode used in this study was ~12 to 14 mA·hour cm^{-2}.

For planar Li foil, the large volume change during cycling and the uneven Li plating/stripping make it difficult to maintain a continuous adhesive contact with the CPE (Fig. 3A). The solid electrolyte delamination will increase the interfacial resistance of the cells during cycling, resulting in augmenting overpotential (*39*). For our novel anode design, a much lesser degree of interfacial fluctuation can be expected because of the high surface area (interfacial fluctuation can be reduced to the submicrometer scale, as calculated from the exchange current density; fig. S8), and the fluidic PEG interphase layer could also continuously adjust its conformation during cycling, both of which are beneficial to afford an intimate electrode-electrolyte contact (Fig. 3B). In addition, the high–surface area Li can also effectively dissipate the local current density to reduce the charge transfer resistance. We believe that when Li is stripped from the inside of 3D Li-rGO, the flowable interphase can partially fill the empty spaces left behind and therefore maintain the ionic contact between the anode surface and the solid electrolyte. During subsequent Li deposition, Li metal can squeeze the flowable interphase due to the softness of this polymer electrolyte layer and deposit back into the 3D porous electrode. Because not all the Li is stripped away, the remaining Li inside Li-rGO can provide a strong

driving force for Li to be deposited back into the electrode due to the much lower Li nucleation barrier on the Li surface.

Correspondingly, as can be seen in Fig. 3C, the Li-rGO symmetric cells consistently showed a much smaller Li stripping/plating polarization compared to the Li foil cells at 60°C. Noticeably, Li foil cannot be operated at a current density of 1 mA cm^{-2} due to interphase delamination (overpotential increased to above 5 V), whereas the Li-rGO cells still exhibited stable voltage profiles. At a current density of 0.1 mA cm^{-2} (Fig. 3D), the average overpotential for Li-rGO cells was 24 mV, which is only one-fourth the value of Li foil cells (~95 mV). The advantages became more obvious at higher current densities. For example, when cycled at a current density of 0.5 mA cm^{-2}, the average overpotential of the Li foil cells was as high as 425 mV, whereas the value for Li-rGO cells was only 125 mV (Fig. 3E). Moreover, the 3D Li-rGO anode with flowable interphase also greatly outperformed the conventional Li foil in terms of cycling stability. As shown in Fig. 3F, the Li-rGO symmetric cells exhibited stable cycling for at least 300 cycles (900 hours) at a current density of 0.5 mA cm^{-2}, and no observable dendrites can be found on the surface of the Li-rGO electrode after cycling (fig. S9). On the other hand, at the same current density, the Li foil cells showed gradual increase in voltage hysteresis over cycles due to the accu-

mulating interfacial impedance, followed by internal short circuit within only 43 cycles.

To account for the improved electrochemical performance, separate experiments were further designed to elucidate the contributions of both the flowable PEG interphase and the high–surface area 3D Li-rGO anode. To demonstrate the importance of having a flowable interfacial layer to continuously adjust its conformation during cycling, flowable PEG was replaced with a relatively rigid cross-linked polymer electrolyte interphase. This cross-linked interphase was obtained by infiltrating an electrolyte precursor composed of 6:4:8 (weight ratio) poly(ethylene glycol) diacrylate [PEGDA; M_W, ~700, with 1 weight % (wt %) Ciba Irgacure 819]/succinonitrile (as a plasticizer)/LiTFSI into the 3D Li-rGO electrode followed by photocuring under a 360-nm ultraviolet light. As shown in fig. S10, 3D Li-rGO with cross-linked PEGDA interphase exhibited a higher Li stripping/plating overpotential compared to that with flowable PEG interphase, which justified the claim that an adaptable interfacial layer can be indispensable in improving the electrode-electrolyte contact in solid-state cells. Symmetric cell cycling was also performed using planar Li foil electrodes with 10 μl of flowable PEG covered on the surface (Li foil–flowable PEG; fig. S11). To some degree, the presence of the flowable PEG improved the adhesion
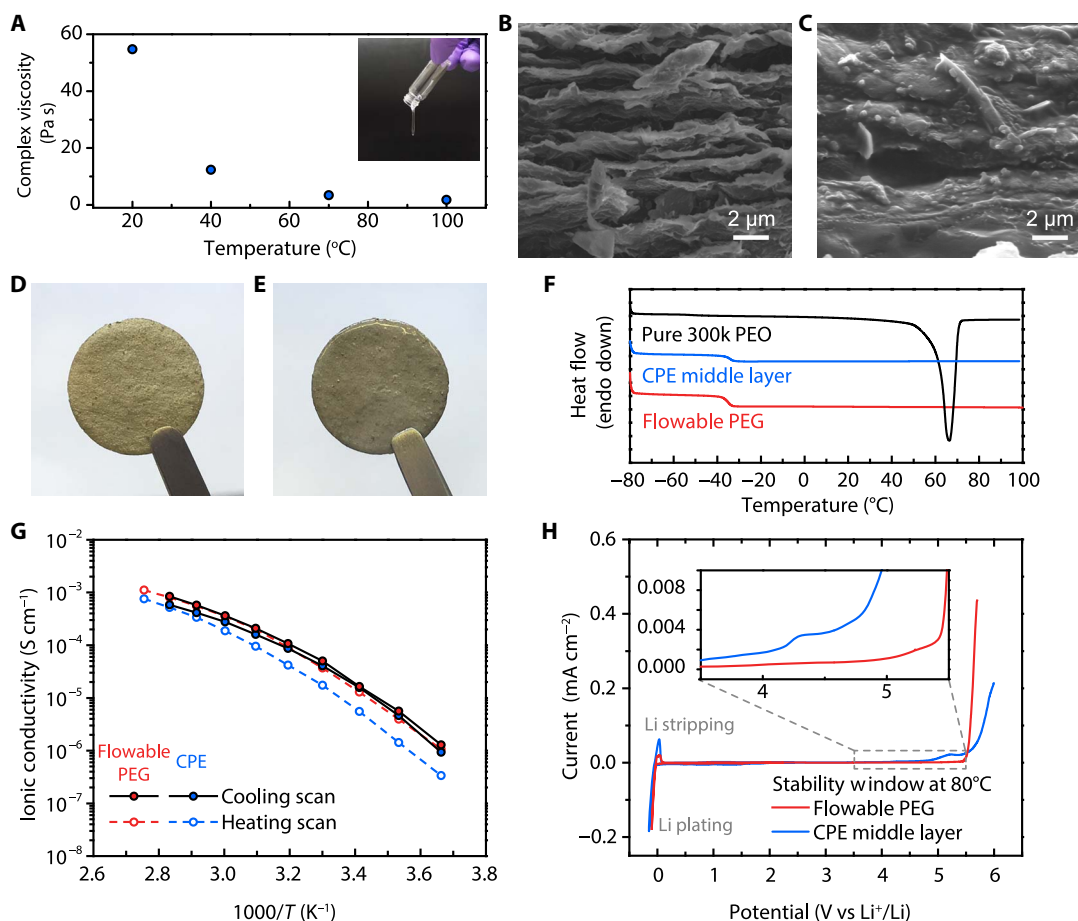

Fig. 2. Characterizations of the flowable PEG and the CPE middle layer. (**A**) Complex viscosity of the flowable PEG as a function of time at 10 Hz obtained via rheology measurements. Inset: Digital photo image of the flowable PEG at room temperature. SEM and digital photo images of the 3D Li-rGO anode (**B** and **D**) before and (**C** and **E**) after thermal infiltration of the flowable PEG. (**F**) DSC thermograms of pure PEO, CPE middle layer, and flowable PEG. The endothermic peak of pure PEO at ~65°C corresponds to the melting of crystalline PEO. Ionic conductivity (**G**) and electrochemical stability window (**H**) of the flowable PEG and the CPE middle layer. The CV scans for the determination of the electrochemical stability windows were carried out at a scan rate of 0.1 mV s^{-1}.
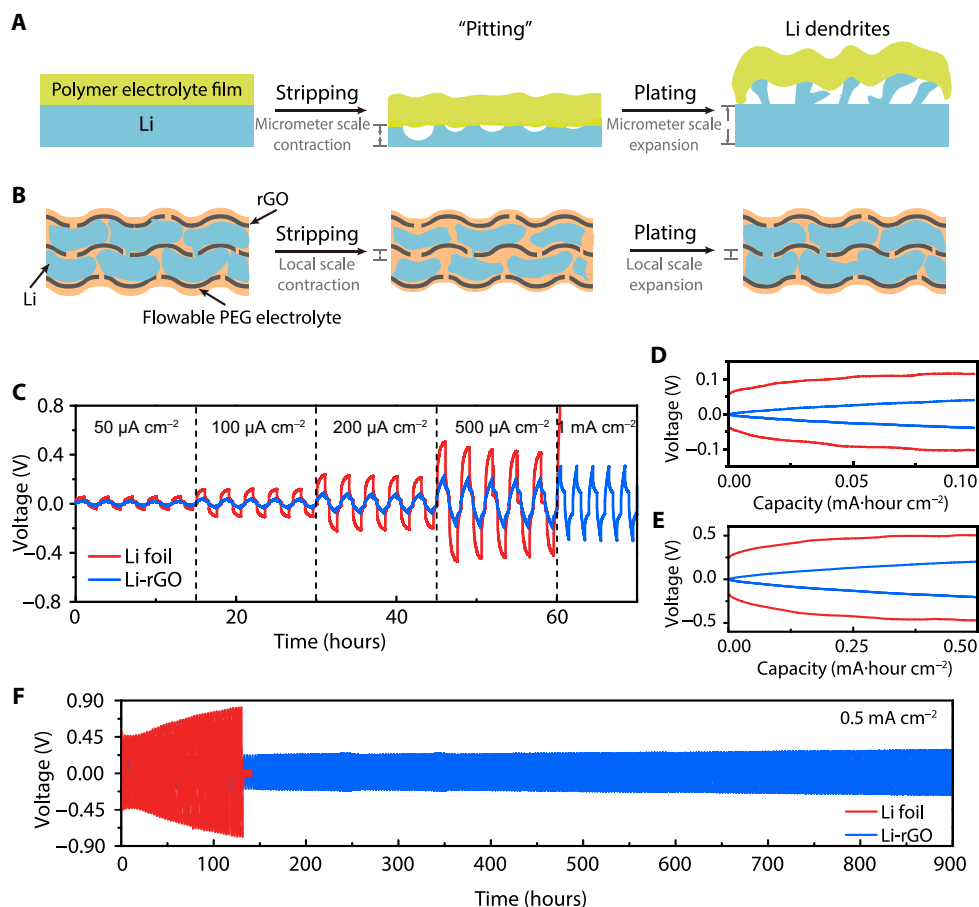
Fig. 3. Galvanostatic cycling of symmetric cells using 3D Li-rGO with flowable interphase and planar Li foil electrodes at 60°C. (**A**) Schematic illustrating the micrometer-scale volume change and uneven Li stripping/plating of Li foil anode, which make it challenging for the solid electrolyte to maintain a continuous contact during cycling. As a "hostless" electrode, the volume of the electrode contracts and expands during Li stripping and plating, respectively. For a practical battery, the areal capacity of a single-sided electrode is ~3 mA·hour cm^{-2}, equivalent to a relative change in thickness of ~15 µm for Li. Moreover, Li tends to be cycled in a nonuniform fashion as localized stripping (pitting) and dendritic plating are often observed. The nonuniform, micrometer-scale electrode-electrolyte interphase movement prevents the formation of a good contact. (**B**) Schematic illustrating the advantages of the 3D Li-rGO anode for solid Li batteries. The significantly reduced interfacial fluctuation due to increased Li surface area and the flowable nature of the interphase polymer electrolyte are beneficial in maintaining an intimate electrode-electrolyte contact during cycling. (**C**) Voltage profiles at different current densities. The charging/discharging time was fixed at 1 hour for all the current densities except 1 mA cm^{-2} (30-min charging/discharging) and with 30-min rest in between. (**D** and **E**) Detailed voltage profiles at a current density of 0.1 and 0.5 mA cm^{-2}, respectively. (**F**) Comparison of the long-term cycling stability of the symmetric cells with Li-rGO electrodes and Li foil electrodes at a current density of 0.5 mA cm^{-2}.

between Li foil and the solid electrolyte middle layer such that a slightly reduced overpotential can be achieved at low current densities. Nevertheless, the performance remained much inferior to that of 3D Li-rGO with flowable interphase. Therefore, it is evident that the combination of 3D Li and the flowable interphase is required to achieve the desirable electrochemical performance.

To corroborate the abovementioned points, the interfacial resistance of the symmetric cells was further evaluated using electrochemical impedance spectroscopy (fig. S12). The partial semicircle at high frequency of the Nyquist plot represents the resistance of the CPE layer, whereas the large semicircle at medium and low frequencies corresponds to the interfacial resistance (R_i). At 60°C, the R_i of the Li foil symmetric cell was ~221 ohm·cm^2 and increased to ~300 ohm·cm^2 after only 20 galvanostatic cycles at a current density of 0.2 mA cm^{-2} and a capacity of 0.2 mA·hour cm^{-2}, indicating the rapidly deteriorating electrode-electrolyte contact during cycling. With a thin flowable PEG layer to improve adhesion, R_i could be reduced to ~108 ohm·cm^2; however,

the value doubled (~205 ohm·cm^2) after 20 cycles due to the micrometer-scale Li stripping/plating volume change that could hardly be accommodated by the thin flowable layer. The 3D Li-rGO cell with flowable interphase exhibited an R_i value of only ~18 ohm·cm^2, which is one order of magnitude smaller than that of the Li foil cells. The result is consistent with the exchange current density measurements, where the electroactive surface area of the 3D Li-rGO electrode was approximated as at least one order of magnitude larger. The increase in interfacial resistance was minimal after cycling (~24 ohm·cm^2), proving the stability of the interphase between 3D Li-rGO and flowable PEG.

When the operating temperature was further increased to 80°C, the Li stripping/plating overpotential of the Li foil cells improved because of both the increased ionic conductivity and the softening of the CPE middle layer, which is beneficial for the adhesive interfacial contact (fig. S13). However, the reduced mechanical property of the CPE layer also made the cells constructed using Li foils more prone to internal short circuit (that is, the Li foil cell shorted at 0.5 mA cm^{-2}). Nevertheless, our
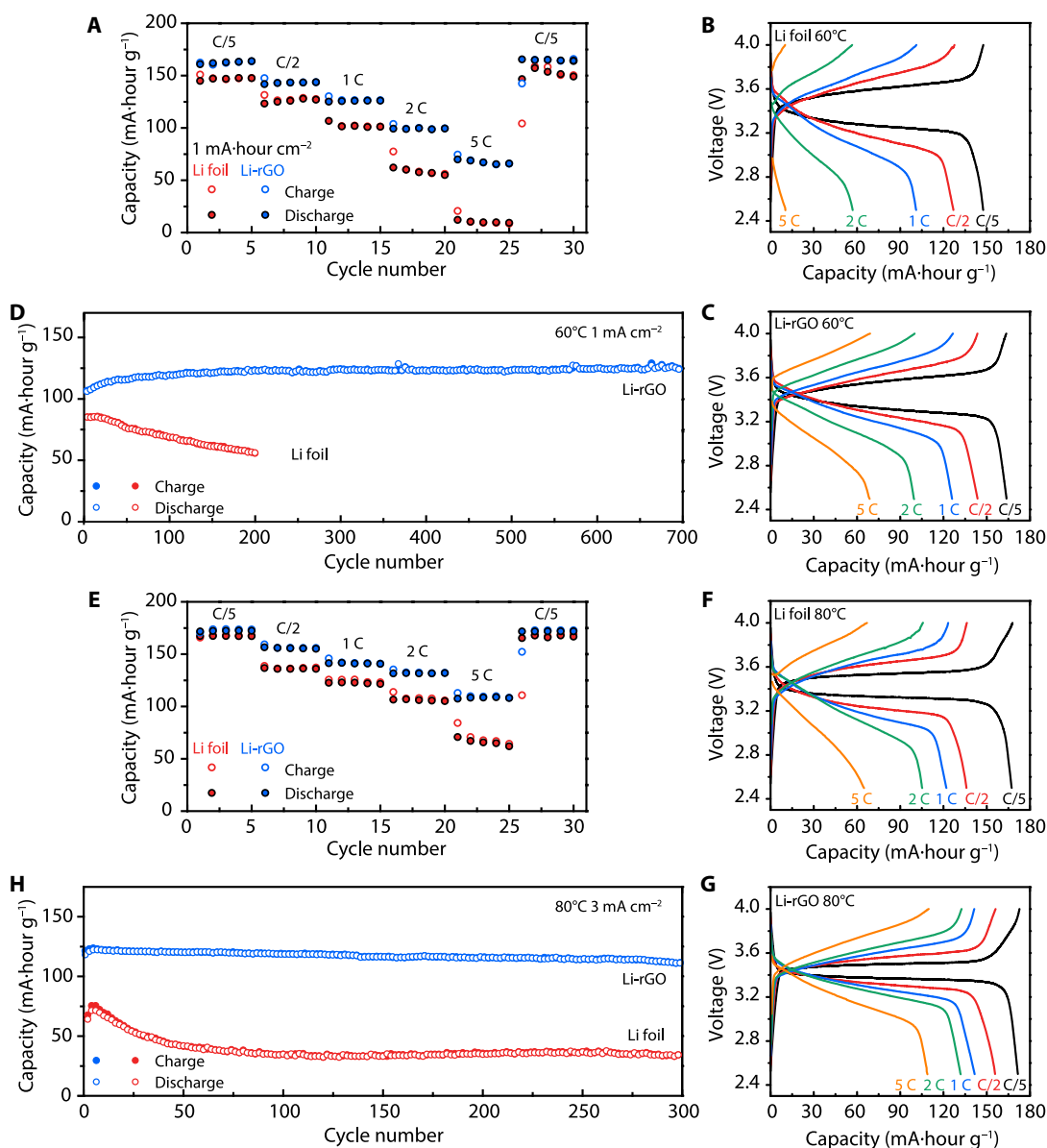
Fig. 4. Electrochemical performance of solid-state Li-LFP batteries with CPE as the middle layer. Rate capability (**A**) and the corresponding galvanostatic charge/discharge voltage profiles (**B** and **C**) of Li-LFP full cells using either 3D Li-rGO or Li foil as the anode at an operating temperature of 60°C. (**D**) Long-term cycling performance of batteries at a current density of 1 mA cm^{-2} and an operating temperature of 60°C. Rate capability (**E**) and the corresponding galvanostatic charge/discharge voltage profiles (**F** and **G**) of Li-LFP full cells using either 3D Li-rGO or Li foil as the anode at an operating temperature of 80°C. (**H**) Long-term cycling performance of batteries at a current density of 3 mA cm^{-2} and an operating temperature of 80°C. The areal capacity of the cathode is ~1 mA·hour cm^{-2} and 1 C = 170 mA g^{-1}.

3D Li cells still excelled in overpotential and long-term stability (figs. S13 and S14). Noticeably, different from the low current density cyclings in most of the previous studies, the Li-rGO cells can be cycled at a high current density of at least 2 mA cm^{-2}. More than 900 hours of stable Li stripping/plating with little overpotential increase can be realized at various current densities and cycling capacities (demonstrated up to 1.5 mA·hour cm^{-2} cycling capacity). This notably improved electrochemical performance compared to that of planar Li foil, especially at high current densities and capacities, justifies the effectiveness of using the 3D Li anode with flowable interphase for high-performance solid Li batteries.

Solid-state Li-LFP cells with CPE middle layer
To demonstrate the feasibility of our novel 3D Li anode design for solid-state Li battery, full cells paired with LFP cathode and CPE middle layer were first assembled to carefully examine the rate capability and long-term cycling stability. Notably, different from many previous studies on solid Li batteries where the cathode mass loading was kept low to minimize the interfacial delamination (36, 40, 41), a relatively high capacity cathode (~1 mA·hour cm^{-2}) was used here to highlight the effectiveness of our design strategy toward improving the interfacial contact. As can be seen from Fig. 4A, it is apparent that a full cell using the 3D Li-rGO anode demonstrated much better rate performance
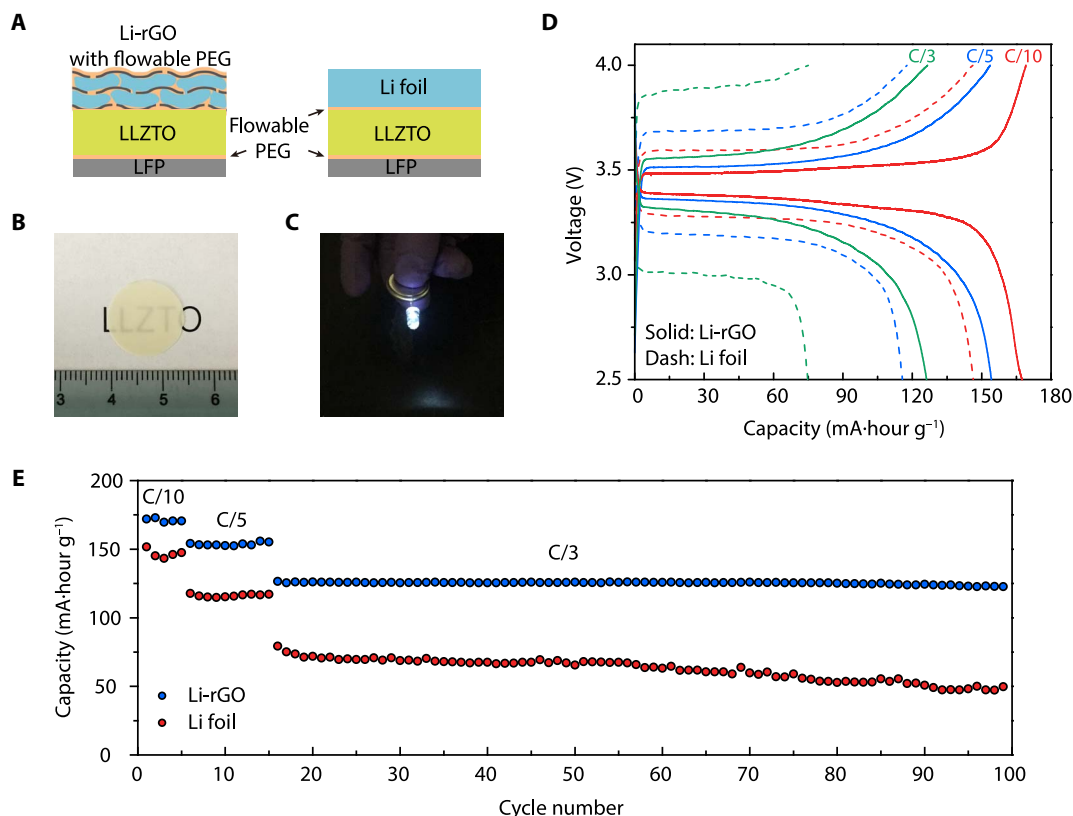
Fig. 5. Electrochemical performance of solid-state Li-LFP batteries with LLZTO as the middle layer. (**A**) Schematic of the solid-state cells with 3D Li-rGO or Li foil anode, LLZTO solid electrolyte middle layer, and LFP cathode. Note that 10 μl of flowable PEG was introduced on top of the Li foil and LFP cathode to improve the interfacial adhesion. (**B**) Digital photo image of the translucent polished LLZTO membrane. (**C**) Working solid-state cell using 3D Li-rGO with flowable interphase as the anode lighting up a light-emitting diode device. Galvanostatic charge/discharge voltage profiles (**D**) and cycling performance of Li-LFP full cells (**E**) using either 3D Li-rGO or Li foil as the anode at room temperature.

compared to the Li foil counterpart at 60°C. At relatively low current densities, the specific discharge capacity of the Li foil cell was 147, 127, and 101 mA·hour g^{-1} at 0.2, 0.5, and 1 C, respectively (Fig. 4B), whereas the values of the 3D Li-rGO cell can be as high as 164, 144, and 126 mA·hour g^{-1} at 0.2, 0.5, and 1 C, respectively (Fig. 4C). The discrepancy was even larger at increased current densities. The discharge capacity of the Li foil cell dropped to 57 mA·hour g^{-1} at 2 C and to only 10 mA·hour g^{-1} at 5 C due to the limited electroactive surface area, whereas decent capacities can still be retained for the Li-rGO cell (100 and 70 mA·hour g^{-1} at 2 and 5 C, respectively), which is important for advanced applications. With regard to the long-term cycling stability, over 700 charge/discharge cycles can be achieved using the 3D Li-rGO anode with no degradation (Fig. 4D), whereas the capacity of the Li foil cell decayed rapidly with 200 cycles due to the incrementing interfacial impedance reflected from the more polarized voltage profiles (fig. S15).

The 3D Li-rGO full cells with flowable interphase presented even better performance at 80°C. They could deliver capacities of 170, 156, 141, 132, and 110 mA·hour g^{-1} at varied rates of 0.2, 0.5, 1, 2, and 5 C, respectively, which were much better than cells using the Li foil anode (Fig. 4, E to G). Noticeably, long-term cycling at a high current density of 3 mA cm^{-2} can deliver an initial discharge capacity of 125 mA·hour g^{-1} with 93.6% capacity retention after 300 cycles (117 mA·hour g^{-1}), whereas the Li foil counterpart only preserved 46% of its initial capacity (72 mA·hour g^{-1}) after 300 cycles (Fig. 4H). Superior cycling stabilities

were also demonstrated at other current densities (fig. S16). The coulombic efficiency data of the LFP cells corresponding to Fig. 4 (D and H) are provided in fig. S17. It is evident that the coulombic efficiency of the 3D Li-rGO cells demonstrated very stable coulombic efficiency during cycling with values approaching 100%, whereas the values of Li foil cells were much lower and much more scattered. Finally, full cells operating at lower temperatures are also possible using the 3D Li-rGO anode, whereas the Li foil cells barely showed any capacity (40°C, fig. S18). By taking into account both the cycling capacity and the current density, the full-cell performance in this study is among the best reported so far (table S1). The remarkable electrochemical data are a strong indicator of the superior interfacial properties using our 3D Li-rGO anode with flowable interphase.

At lower temperatures, the electrochemical performance is mainly restricted by the limited ionic conductivity of the CPE middle layer. To prove the point, the CPE middle layer is replaced by cross-linked PEGDA electrolyte, whose ionic conductivity is higher at room temperature. As a result, stable cycling can be successfully demonstrated at room temperature with much reduced overpotential than the Li foil counterpart (fig. S19).

Solid-state Li-LFP cells with ceramic electrolyte middle layer
Finally, because the aim of this work is to demonstrate an effective strategy to solve the interfacial impedance issue in solid Li batteries from an electrode structural design perspective, it is important to

prove the general applicability of this 3D Li anode design. Correspondingly, the Li-rGO anode with flowable interphase was also used in Li-LFP cells with a cubic garnet-type LLZTO ceramic electrolyte middle layer (fig. S20) (42, 43). Li-LFP coin cells with LLZTO middle layer were constructed following the schematic shown in Fig. 5A (cathode active material has a mass loading of ~1.5 mg cm^{-2}). A thin layer (10 μl) of flowable PEG was introduced on both Li foil and LFP cathode to reduce the interfacial resistance. Figure 5B shows the digital photo image of the translucent LLZTO pellet, which was ~400 μm thick. When operated at room temperature (Fig. 5C), the Li-LFP cells using the 3D Li metal anode demonstrated much lower charge/discharge overpotential and specific capacity compared to the Li foil reference cells (Fig. 5D). Moreover, significantly improved rate capability and cycling stability can also be observed when replacing the conventional Li foil with the novel 3D Li anode design (Fig. 5E). Therefore, our 3D Li metal anode with flowable interphase is highly promising for general applications in conjunction with different solid electrolyte systems to answer the interfacial impedance challenge in solid-state Li metal batteries.

CONCLUSIONS

To summarize, the large interfacial resistance of solid-state Li metal batteries caused by the poor Li-solid electrolyte adhesion is an outstanding roadblock to their high-power and high-capacity operations. Although the development of better solid electrolytes is crucial in addressing this challenge, it can be equally important to improve the structural design of solid-state Li metal batteries by leveraging the advances in nanomaterial synthesis. However, the latter has not been much accounted for by the battery community. In an attempt to fill the gap, a new approach is presented in this study to tackle the problem of Li-solid electrolyte adhesion: Whereas all the previous studies were based on planar Li foil, we adopted a 3D Li anode for the first time for the construction of solid Li batteries. The high–surface area Li can significantly reduce the effective current density and the degree of volumetric change, giving rise to improved battery kinetics and reduced possibility of electrolyte delamination. The 3D Li anode surface was ionically connected to the bulk solid electrolyte via a flowable polymer electrolyte interphase, which is crucial for accommodating the interfacial fluctuation during cycling to maintain an intimate contact. As a consequence, significantly reduced overpotential and greatly improved cycling stability were realized in both symmetric and full-cell configurations. The adoption of the 3D Li anode with flowable interphase proves a promising design principle and can open up new possibilities for the next-generation high-energy solid-state Li batteries and their safe operation.

MATERIALS AND METHODS

Fabrication of the 3D Li-rGO electrode with flowable interphase

The composite Li metal-rGO electrode was fabricated according to our previous report (26) and punched into 1-cm^2 discs (thickness, ~100 to 150 μm). The flowable interphase layer was subsequently obtained via thermal infiltration of molten SPE into the 3D Li-rGO electrode. PEG (M_W, 10,000; Sigma-Aldrich) and LiTFSI (Sigma-Aldrich, 99.95%) were mixed in an 8:1 [EO]/[Li] ratio and heated on a hot plate at 150°C with gentle stirring to afford a homogeneous molten SPE. The Li-rGO electrode was then immersed into the molten SPE, and the infiltration process was carried out under vacuum for ap-

proximately 15 min. Finally, the excess SPE on the surface of the Li-rGO electrode was removed using polyester clean room swabs. The whole fabrication process was carried out in an argon-filled glove box with sub-ppm (parts per million) O_2 and H_2O levels (Vigor Tech).

Fabrication of the CPE middle layer

To fabricate the CPE middle layer, 0.6 g of PEO (M_W, 300,000; Sigma-Aldrich) was dissolved in 10 g of acetonitrile (anhydrous, 99.8%; Sigma-Aldrich) under vigorous stirring. Then, 0.06 g of fumed silica (~14 nm; Sigma-Aldrich) was added, and the mixture was stirred for at least 2 days to afford a homogeneous solution. Subsequently, LiTFSI salt was added in an 8:1 [EO]/[Li] ratio, and the solution was stirred until the salt was well dissolved. The CPE solution was then casted into a Teflon evaporating dish (63 mm in diameter; Fisher Scientific), and the solvent was evaporated naturally over a period of approximately 1 day. The as-obtained CPE was further baked on an 80°C hot plate for at least 3 days to remove a trace amount of water. The cross-linked PEGDA electrolyte was fabricated by photocuring an electrolyte precursor composed of 6:4:8 (weight ratio) PEGDA (M_W, ~700; with 1 wt % Ciba Irgacure 819)/succinonitrile/LiTFSI under a 360-nm ultraviolet light. This electrolyte precursor can also be infiltrated into the 3D porous Li-rGO electrode followed by photocuring to construct a relatively rigid interphase. The whole fabrication process was carried out in an argon-filled glove box with sub-ppm O_2 and H_2O levels.

Fabrication of the ceramic electrolyte middle layer

The cubic garnet-type LLZTO ceramic electrolyte was synthesized by conventional solid-state reaction of stoichiometric amounts of Li_2CO_3 (99.99%, with 20% excess; Sinopharm Chemical Reagent), La_2O_3 (99.99%, dried at 900°C for 12 hours; Sinopharm Chemical Reagent), ZrO_2 (99.99%; Aladdin), and Ta_2O_5 (99.99%; Ourchem). The starting materials were fully grounded with agate mortar and pestle and then heated at 900°C for 6 hours to decompose the metal salts. The resulting powders were then ball-milled with 1.2 wt % of Al_2O_3 for 12 hours and pressed into a pellet under 60-MPa cold isostatic pressing for 120 s. The pellet was placed in an alumina crucible, covered with mother powder, and sintered at 1140°C for 16 hours in an air atmosphere. To obtain the LLZTO membranes, the sintered LLZTO pellet was sliced using a low-speed diamond saw, and the thickness of the LLZTO membranes was ~400 μm. The surface of the LLZTO membranes was polished in an argon-filled glove box with sub-ppm O_2 and H_2O levels using polishing papers with a grit number of 600 before use.

Fabrication of the LFP cathode

LFP powders (MTI Inc.) and Ketjenblack (EC-300J; AkzoNobel) were first dried in vacuum oven at 60°C for 24 hours to remove trapped water. CPE (PEO, LiTFSI, and fumed silica, same as described above) dissolved in acetonitrile was used as the binder. To prepare the LFP electrode, LFP, CPE, and Ketjenblack in a ratio of 65:20:15 were dispersed in acetonitrile and homogenized using a planetary centrifugal mixer (THINKY MIXER ARE-310). The slurry was then uniformly coated on Al foil via doctor blading. The active material mass loading was controlled to be ~6.0 mg cm^{-2}. The LFP cathode was dried at 80°C for at least 3 days inside an argon-filled glove box with sub-ppm O_2 and H_2O levels before use.

Characterizations

The SEM images were taken with a FEI XL30 Sirion scanning electron microscope. The DSC measurement was carried out with a TA

Instrument Q2000 differential scanning calorimeter. The samples were sealed in hermetic aluminum pans (Tzero) and first equilibrated at −80°C. The second heating curves at a ramping rate of 5°C min^{-1} were collected. The rheological properties of the PEG electrolyte were measured using a high-resolution 25-mm parallel-plate rheometer (TA Instrument ARES-G2) with a gap of 0.5 mm. Oscillation sweep was performed at 1% strain at various temperatures. X-ray diffraction patterns were recorded on a PANalytical X'Pert instrument. For the imaging of the electrode surface after cycling, focused ion beam (FIB) was used to mill away the polymer electrolyte on the surface, which was carried out using an FEI Strata 235DB dual-beam FIB/SEM with gallium ion source.

The porosity of the Li-rGO anode was tested via mineral oil absorption. The weight of the Li-rGO electrodes (1 cm^2, ~5 mg) was measured first and then immersed into mineral oil (Light, Fisher Chemical) for 10 min to ensure the complete infiltration of mineral oil into the pores of Li-rGO. Then, the mineral oil that infiltrated the Li-rGO electrodes was carefully wiped with Kimwipes (Kimtech Science) to completely remove the surface mineral oil residue before weighing. Because the densities of Li (0.534 g cm^{-3}) and mineral oil (0.83 g cm^{-3}) are known, we can calculate the volume fraction of mineral oil (occupying the pore space) within the Li-rGO electrodes.

Electrochemical testing

For the ionic conductivity measurement, symmetric stainless steel/polymer electrolyte/stainless steel cells were assembled and measurements were made every 10°C ranging from 0° to 90°C. For electrochemical stability window measurement, Li/polymer electrolyte/stainless steel cells were assembled and the CV was scanned first to negative direction at a scan rate of 0.1 mV s^{-1}. For the exchange current density measurement, a three-electrode Swagelok cell was used. A half-charged LFP electrode was used as the reference, and the working and counter electrodes are both the materials of interest. Linear scan voltammetry was carried out at a scan rate of 0.1 mV s^{-1}. At low current, the Butler-Volmer equation can be approximated to the linear relationship $i \approx i_0 \frac{F}{RT} \eta$, where η is the overpotential. The exchange current i_0 can be extracted from the slope of the η-i curve. For solid-state symmetric cells, the CPE middle layer was sandwiched between the Li metal foils (0.75 mm, 99.9%; Alfa Aesar) and the 3D Li-rGO electrode with flowable interphase. For solid-state full cells, the CPE middle layer or the LLZTO membrane was sandwiched between the Li metal foil/3D Li-rGO electrode with flowable interphase and the LFP cathode. Electrochemical impedance measurements were carried out in coin cells on a Bio-Logic VMP3 system. Galvanostatic cycling was conducted on a standard eight-channel battery tester (Wuhan LAND Electronics Co. Ltd.). The temperature of the cells was controlled by an environmental chamber (BTU-133, ESPEC North America Inc.) with a precision of ±0.1°C.

SUPPLEMENTARY MATERIALS

Supplementary material for this article is available at http://advances.sciencemag.org/cgi/content/full/3/10/eaao0713/DC1

fig. S1. Fabrication of the 3D porous Li-rGO composite anode.
fig. S2. SEM images of the bulk CPE.
fig. S3. Ionic conductivities at different temperatures and photo images of PEG-LiTFSI with varying [EO]/[Li] ratios.
fig. S4. Rheological properties of flowable PEG.
fig. S5. Porosity of the 3D porous Li-rGO anode.
fig. S6. Specific capacity of the 3D porous Li-rGO anode.
fig. S7. Cross-sectional SEM images of the 3D porous Li-rGO anode with different thickness.
fig. S8. Comparison of the exchange currents of Li foil and Li-rGO.

fig. S9. FIB/SEM images of Li foil and 3D Li-rGO electrode after cycling.
fig. S10. The effect of flowable interphase.
fig. S11. The effect of high–surface area Li.
fig. S12. Electrochemical impedance study.
fig. S13. Symmetric cell voltage profiles at 80°C.
fig. S14. Cycling stability of symmetric cells at 80°C.
fig. S15. Voltage profiles of Li-LFP full cells after cycling.
fig. S16. Cycling stability of Li-LFP cells at 80°C.
fig. S17. Coulombic efficiency of Li-LFP cells.
fig. S18. The electrochemical performance of Li-LFP full cells at 40°C.
fig. S19. The electrochemical performance of symmetric cells with PEGDA middle layer at room temperature.
fig. S20. Characterizations on the LLZTO membranes.
table S1. Comparison of the electrochemical performance of our solid-state Li battery using 3D Li with flowable interphase with those reported in the literature using the Li foil anode.
References (44–51)

REFERENCES AND NOTES

1. J.-M. Tarascon, M. Armand, Issues and challenges facing rechargeable lithium batteries. *Nature* **414**, 359–367 (2001).
2. M. Armand, J.-M. Tarascon, Building better batteries. *Nature* **451**, 652–657 (2008).
3. P. G. Bruce, S. A. Freunberger, L. J. Hardwick, J.-M. Tarascon, Li–O$_2$ and Li–S batteries with high energy storage. *Nat. Mater.* **11**, 19–29 (2012).
4. C. P. Grey, J. M. Tarascon, Sustainability and in situ monitoring in battery development. *Nat. Mater.* **16**, 45–56 (2017).
5. W. Xu, J. Wang, F. Ding, X. Chen, E. Nasybulin, Y. Zhang, J.-G. Zhang, Lithium metal anodes for rechargeable batteries. *Energy Environ. Sci.* **7**, 513–537 (2014).
6. G. Zheng, S. W. Lee, Z. Liang, H.-W. Lee, K. Yan, H. Yao, H. Wang, W. Li, S. Chu, Y. Cui, Interconnected hollow carbon nanospheres for stable lithium metal anodes. *Nat. Nanotechnol.* **9**, 618–623 (2014).
7. A. Varzi, R. Raccichini, S. Passerini, B. Scrosati, Challenges and prospects of the role of solid electrolytes in the revitalization of lithium metal batteries. *J. Mater. Chem. A* **4**, 17251–17259 (2016).
8. J. Motavalli, Technology: A solid future. *Nature* **526**, S96–S97 (2015).
9. C. Monroe, J. Newman, The impact of elastic deformation on deposition kinetics at lithium/polymer interfaces. *J. Electrochem. Soc.* **152**, A396–A404 (2005).
10. R. Murugan, V. Thangadurai, W. Weppner, Fast lithium ion conduction in garnet-type Li$_7$La$_3$Zr$_2$O$_{12}$. *Angew. Chem. Int. Ed.* **46**, 7778–7781 (2007).
11. E. G. Herbert, W. E. Tenhaeff, N. J. Dudney, G. M. Pharr, Mechanical characterization of LiPON films using nanoindentation. *Thin Solid Films* **520**, 413–418 (2011).
12. N. Kamaya, K. Homma, Y. Yamakawa, M. Hirayama, R. Kanno, M. Yonemura, T. Kamiyama, Y. Kato, S. Hama, K. Kawamoto, A. Mitsui, A lithium superionic conductor. *Nat. Mater.* **10**, 682–686 (2011).
13. Y. Kato, S. Hori, T. Saito, K. Suzuki, M. Hirayama, A. Mitsui, M. Yonemura, H. Iba, R. Kanno, High-power all-solid-state batteries using sulfide superionic conductors. *Nat. Energy* **1**, 16030 (2016).
14. Y. Zhu, X. He, Y. Mo, Origin of outstanding stability in the lithium solid electrolyte materials: Insights from thermodynamic analyses based on first-principles calculations. *ACS Appl. Mater. Interfaces* **7**, 23685–23693 (2015).
15. W. D. Richards, L. J. Miara, Y. Wang, J. C. Kim, G. Ceder, Interface stability in solid-state batteries. *Chem. Mater.* **28**, 266–273 (2015).
16. M. Armand, Polymer solid electrolytes—An overview. *Solid State Ion.* **9–10**, 745–754 (1983).
17. R. Bouchet, S. Maria, R. Meziane, A. Aboulaich, L. Lienafa, J.-P. Bonnet, T. N. T. Phan, D. Bertin, D. Gigmes, D. Devaux, R. Denoyel, M. Armand, Single-ion BAB triblock copolymers as highly efficient electrolytes for lithium-metal batteries. *Nat. Mater.* **12**, 452–457 (2013).
18. Z. Xue, D. He, X. Xie, Poly(ethylene oxide)-based electrolytes for lithium-ion batteries. *J. Mater. Chem. A* **3**, 19218–19253 (2015).
19. T. Matsui, K. Takeyama, Lithium deposit morphology from polymer electrolytes. *Electrochim. Acta* **40**, 2165–2169 (1995).
20. X.-X. Zeng, Y.-X. Yin, N.-W. Li, W.-C. Du, Y.-G. Guo, L.-J. Wan, Reshaping lithium plating/stripping behavior via bifunctional polymer electrolyte for room-temperature solid Li metal batteries. *J. Am. Chem. Soc.* **138**, 15825–15828 (2016).
21. L. Porcarelli, C. Gerbaldi, F. Bella, J. R. Nair, Super soft all-ethylene oxide polymer electrolyte for safe all-solid lithium batteries. *Sci. Rep.* **6**, 19892 (2016).
22. X. Han, Y. Gong, K. Fu, X. He, G. T. Hitz, J. Dai, A. Pearse, B. Liu, H. Wang, G. Rubloff, Y. Mo, V. Thangadurai, E. D. Wachsman, L. Hu, Negating interfacial impedance in garnet-based solid-state Li metal batteries. *Nat. Mater.* **16**, 572–579 (2017).

23. W. Zhou, S. Wang, Y. Li, S. Xin, A. Manthiram, J. B. Goodenough, Plating a dendrite-free lithium anode with a polymer/ceramic/polymer sandwich electrolyte. *J. Am. Chem. Soc.* **138**, 9385–9388 (2016).

24. P. R. Chinnam, S. L. Wunder, Engineered interfaces in hybrid ceramic–polymer electrolytes for use in all-solid-state Li batteries. *ACS Energy Lett.* **2**, 134–138 (2016).

25. G. M. Stone, S. A. Mullin, A. A. Teran, D. T. Hallinan Jr., A. M. Minor, A. Hexemer, N. P. Balsara, Resolution of the modulus versus adhesion dilemma in solid polymer electrolytes for rechargeable lithium metal batteries. *J. Electrochem. Soc.* **159**, A222–A227 (2012).

26. D. Lin, Y. Liu, Z. Liang, H.-W. Lee, J. Sun, H. Wang, K. Yan, J. Xie, Y. Cui, Layered reduced graphene oxide with nanoscale interlayer gaps as a stable host for lithium metal anodes. *Nat. Nanotechnol.* **11**, 626–632 (2016).

27. Y. Liu, D. Lin, Z. Liang, J. Zhao, K. Yan, Y. Cui, Lithium-coated polymeric matrix as a minimum volume-change and dendrite-free lithium metal anode. *Nat. Commun.* **7**, 10992 (2016).

28. Z. Liang, D. Lin, J. Zhao, Z. Lu, Y. Liu, C. Liu, Y. Lu, H. Wang, K. Yan, X. Tao, Y. Cui, Composite lithium metal anode by melt infusion of lithium into a 3D conducting scaffold with lithiophilic coating. *Proc. Natl. Acad. Sci. U.S.A.* **113**, 2862–2867 (2016).

29. Y. Sun, G. Zheng, Z. W. Seh, N. Liu, S. Wang, J. Sun, H. R. Lee, Y. Cui, Graphite-encapsulated Li-metal hybrid anodes for high-capacity Li batteries. *Chem* **1**, 287–297 (2016).

30. R. Zhang, X.-B. Cheng, C.-Z. Zhao, H.-J. Peng, J.-L. Shi, J.-Q. Huang, J. Wang, F. Wei, Q. Zhang, Conductive nanostructured scaffolds render low local current density to inhibit lithium dendrite growth. *Adv. Mater.* **28**, 2155–2162 (2016).

31. Z. Liu, W. Fu, E. A. Payzant, X. Yu, Z. Wu, N. J. Dudney, J. Kiggans, K. Hong, A. J. Rondinone, C. Liang, Anomalous high ionic conductivity of nanoporous β-Li$_3$PS$_4$. *J. Am. Chem. Soc.* **135**, 975–978 (2013).

32. Y. Liu, D. Lin, P. Y. Yuen, K. Liu, J. Xie, R. H. Dauskardt, Y. Cui, An artificial solid electrolyte interphase with high Li-ion conductivity, mechanical strength, and flexibility for stable lithium metal anodes. *Adv. Mater.* **29**, 1605531 (2017).

33. A. C. Kozen, C.-F. Lin, A. J. Pearse, M. A. Schroeder, X. Han, L. Hu, S.-B. Lee, G. W. Rubloff, M. Noked, Next-generation lithium metal anode engineering via atomic layer deposition. *ACS Nano* **9**, 5884–5892 (2015).

34. Y. Cao, X. Meng, J. W. Elam, Atomic layer deposition of Li$_x$Al$_y$S solid-state electrolytes for stabilizing lithium-metal anodes. *ChemElectroChem* **3**, 858–863 (2016).

35. F. Croce, G. B. Appetecchi, L. Persi, B. Scrosati, Nanocomposite polymer electrolytes for lithium batteries. *Nature* **394**, 456–458 (1998).

36. D. Lin, W. Liu, Y. Liu, H. R. Lee, P.-C. Hsu, K. Liu, Y. Cui, High ionic conductivity of composite solid polymer electrolyte via in situ synthesis of monodispersed SiO$_2$ nanospheres in poly(ethylene oxide). *Nano Lett.* **16**, 459–465 (2015).

37. J. Cruickshank, H. V. S. A. Hubbard, N. Boden, I. M. Ward, The role of ionic salts in determining T_g and ionic conductivity in concentrated PEG electrolyte solutions. *Polymer* **36**, 3779–3781 (1995).

38. J. F. Vélez, M. Aparicio, J. Mosa, Effect of lithium salt in nanostructured silica–polyethylene glycol solid electrolytes for Li-ion battery applications. *J. Phys. Chem. C* **120**, 22852–22864 (2016).

39. D. Devaux, K. J. Harry, D. Y. Parkinson, R. Yuan, D. T. Hallinan, A. A. MacDowell, N. P. Balsara, Failure mode of lithium metal batteries with a block copolymer electrolyte analyzed by x-ray microtomography. *J. Electrochem. Soc.* **162**, A1301–A1309 (2015).

40. S. Iwasaki, T. Hamanaka, T. Yamakawa, W. C. West, K. Yamamoto, M. Motoyama, T. Hirayama, Y. Iriyama, Preparation of thick-film LiNi$_{1/3}$Co$_{1/3}$Mn$_{1/3}$O$_2$ electrodes by aerosol deposition and its application to all-solid-state batteries. *J. Power Sources* **272**, 1086–1090 (2014).

41. R. Inada, S. Yasuda, M. Tojo, K. Tsuritani, T. Tojo, Y. Sakurai, Development of lithium-stuffed garnet-type oxide solid electrolytes with high ionic conductivity for application to all-solid-state batteries. *Front. Energy Res.* **4**, 28 (2016).

42. L. Cheng, E. J. Crumlin, W. Chen, R. Qiao, H. Hou, S. F. Lux, V. Zorba, R. Russo, R. Kostecki, Z. Liu, K. Persson, W. Yang, J. Cabana, T. Richardson, G. Chen, M. Doeff, The origin of high electrolyte–electrode interfacial resistances in lithium cells containing garnet type solid electrolytes. *Phys. Chem. Chem. Phys.* **16**, 18294–18300 (2014).

43. W. Luo, Y. Gong, Y. Zhu, K. K. Fu, J. Dai, S. D. Lacey, C. Wang, B. Liu, X. Han, Y. Mo, E. D. Wachsman, L. Hu, Transition from superlithiophobicity to superlithiophilicity of garnet solid-state electrolyte. *J. Am. Chem. Soc.* **138**, 12258–12262 (2016).

44. F. Croce, S. Sacchetti, B. Scrosati, Advanced, lithium batteries based on high-performance composite polymer electrolytes. *J. Power Sources* **162**, 685–689 (2006).

45. L. Damen, J. Hassoun, M. Mastragostino, B. Scrosati, Solid-state, rechargeable Li/LiFePO$_4$ polymer battery for electric vehicle application. *J. Power Sources* **195**, 6902–6904 (2010).

46. D. T. Hallinan Jr., S. A. Mullin, G. M. Stone, N. P. Balsara, Lithium metal stability in batteries with block copolymer electrolytes. *J. Electrochem. Soc.* **160**, A464–A470 (2013).

47. Q. Pan, D. M. Smith, H. Qi, S. Wang, C. Y. Li, Hybrid electrolytes with controlled network structures for lithium metal batteries. *Adv. Mater.* **27**, 5995–6001 (2015).

48. Y. Zhao, C. Wu, G. Peng, X. Chen, X. Yao, Y. Bai, F. Wu, S. Chen, X. Xu, A new solid polymer electrolyte incorporating Li$_{10}$GeP$_2$S$_{12}$ into a polyethylene oxide matrix for all-solid-state lithium batteries. *J. Power Sources* **301**, 47–53 (2016).

49. W. Zhou, H. Gao, J. B. Goodenough, Low-cost hollow mesoporous polymer spheres and all-solid-state lithium, sodium batteries. *Adv. Energy Mater.* **6**, 1501802 (2016).

50. M. Agostini, Y. Aihara, T. Yamada, B. Scrosati, J. Hassoun, A lithium–sulfur battery using a solid, glass-type P$_2$S$_5$–Li$_2$S electrolyte. *Solid State Ion.* **244**, 48–51 (2013).

51. X. Yao, D. Liu, C. Wang, P. Long, G. Peng, Y.-S. Hu, H. Li, L. Chen, X. Xu, High-energy all-solid-state lithium batteries with ultralong cycle life. *Nano Lett.* **16**, 7148–7154 (2016).